PHYSICAL REVIEW B **95**, 094505 (2017)

Doping-induced superconductivity of ZrB_2 and HfB_2

N. Barbero,[1,*] T. Shiroka,[1,2] B. Delley,[2] T. Grant,[3] A. J. S. Machado,[3] Z. Fisk,[4] H.-R. Ott,[1,2] and J. Mesot[1,2]
[1]*Laboratorium für Festkörperphysik, ETH Zürich, CH-8093, Zurich, Switzerland*
[2]*Paul Scherrer Institut, CH-5232, Villigen Paul Scherrer Institute, Switzerland*
[3]*Escola de Engenharia de Lorena, Universidade de São Paulo, P.O. Box 116, Lorena, São Paolo, Brazil*
[4]*Department of Physics and Astronomy, University of California at Irvine, California 92697, USA*

(Received 19 December 2016; revised manuscript received 14 February 2017; published 8 March 2017)

Unlike the widely studied s-type two-gap superconductor MgB_2, the chemically similar compounds ZrB_2 and HfB_2 do not superconduct above 1 K. Yet it has been shown that small amounts of self or extrinsic doping (in particular with vanadium), can induce superconductivity in these materials. Based on results of different macroscopic and microscopic measurements, including magnetometry, nuclear magnetic resonance (NMR), resistivity, and muon-spin rotation (μ^+SR), we present a comparative study of $Zr_{0.96}V_{0.04}B_2$ and $Hf_{0.97}V_{0.03}B_2$. Their key magnetic and superconducting features are determined and the results are considered within the theoretical framework of multiband superconductivity proposed for MgB_2. Detailed Fermi surface (FS) and electronic structure calculations reveal the difference between MgB_2 and transition-metal diborides.

DOI: 10.1103/PhysRevB.95.094505

I. INTRODUCTION

Borides, carbides, and nitrides were among the early compound superconductors discovered in the first half of the previous century [1] (see, e.g., Ref. [2] for a recent review). However, it was only in 2001, with the discovery of superconductivity in MgB_2 at 39 K [3], that researchers intensified the search for superconductivity in other diborides. Based on a large number of studies, MgB_2 was identified as a two-band two-gap superconductor. Its peculiar Fermi surface exhibits two-dimensional hole-like cylinders from the $p_{x,y}$ bands, a hole-like tubular network due to the bonding p_z bands, and an electron-like tubular network due to the antibonding p_z bands [4]. Due to this electronic configuration and to a distinct anisotropy of the electron-phonon interaction strength, the electronic excitation spectrum of MgB_2 adopts two gaps in the superconducting phase: a large gap of 7.2 meV in the $p_{x,y}$ (σ) bands, and a small gap of 2.8 meV in the bonding and antibonding p_z (π) bands. At the same time, an upper critical field anisotropy has been observed, with $\mu_0 H_{c2}{}^{c} \sim 30$ T and $\mu_0 H_{c2}{}^{ab} \sim 3$ T at zero temperature [5].

Besides alkaline-earth metals (such as Mg), diborides of other elements have been proposed to be checked for superconductivity. Because of the presence of partially filled $3d$, $4d$, and $5d$ orbitals, considered as promising for superconductivity, these new attempts involved icosagens (Al) and various d-type transition metals (T). The second of these (TB_2), which are claimed to combine average coupling constants with comparable phonon frequencies to MgB_2 [6] (due to the presence of light boron atoms), were the natural candidates in this search. Unfortunately, these renewed efforts proved unsuccessful and to date there are no reports of superconductivity for the majority of TB_2 materials.

ZrB_2 and HfB_2 are two such nonsuperconducting refractory materials with melting points of ~3000 K, behaving essentially as Pauli paramagnets down to low temperatures. The electrons in the $4d$ shell of zirconium (Zr) and those in the $5d$ shell of hafnium (Hf) are less localized than those of the $3d$ row. In a recent study [7] it was found that by replacing small amounts of Zr or Hf with V, the resulting compounds $Zr_{1-x}V_xB_2$ and $Hf_{1-x}V_xB_2$ are superconductors. Maximum superconducting temperatures $T_c = 8.33$ K and 7.31 K were reached in $Zr_{0.96}V_{0.04}B_2$ and $Hf_{0.97}V_{0.03}B_2$, respectively, at the upper solubility limit of V ($x \approx 0.04$). X-ray powder diffraction (XRD) patterns [7] indicate that an increase in V doping does not change the in-plane lattice parameter a, while it reduces the interlayer distance c. At the same time, it has been shown that the structural and electronic properties of these compounds are influenced by the presence of B vacancies [8].

In Ref. [7], the properties of superconducting $Zr_{0.96}V_{0.04}B_2$ were investigated by means of macroscopic techniques [7]. In this work we aimed at combining macroscopic and microscopic techniques (including magnetometry, NMR, resistivity, and preliminary μ^+SR experiments) on Zr-based diborides and extend our study to include the Hf-based compound. Since we succeeded in synthesizing samples with less magnetic impurities (below 10 ppm) with respect to the previous ones [7], whenever relevant, a comparison between the two batches is included. Our extensive data sets allowed us to unravel clear analogies and differences between the T-diborides $Zr_{0.96}V_{0.04}B_2$ and $Hf_{0.97}V_{0.03}B_2$ and the well-known MgB_2. In Sec. IV A we show that spin-lattice relaxation processes in T-diborides are two orders of magnitude slower that in MgB_2, indicating significantly different electronic structures. Combined magnetometry (Sec. IV B) and resistivity (Sec. IV C) measurements were performed to evaluate the upper and lower critical fields, respectively. These compounds prove to be extreme type-II superconductors, as reflected by the high values (~100) of the Ginzburg-Landau $\kappa = \lambda/\xi$ parameter. The London penetration depth λ was evaluated through μ^+SR (Sec. IV D) experiments and the coherence length ξ via upper critical field measurements (Sec. IV C). Thanks to the complementarity of the used techniques, we argue that, besides the qualitatively different Fermi surfaces of MgB_2 and transition-metal diborides, in both cases we are dealing with s-wave superconductors. While the rather high T_c of MgB_2 is understood as a consequence of a favorable electronic structure

---

[*] Corresponding author: nbarbero@phys.ethz.ch

©2017 American Physical Society

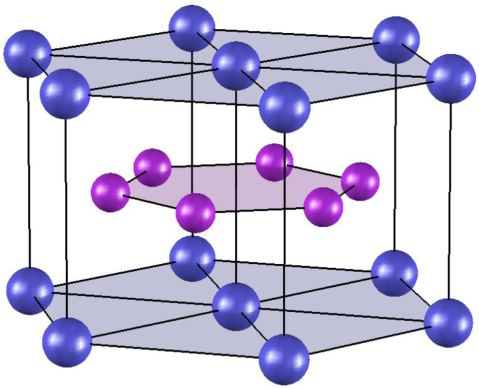

FIG. 1. AlB_2 structure of the transition-metal diborides highlighting the graphene-like B layers (magenta atoms) and the hexagonal metal layers (blue atoms).

and electron-phonon interaction, the drastic effect of V-doping in the T-diborides is still rather surprising.

II. ELECTRONIC STRUCTURES OF ZrB_2 AND HfB_2

Both pure and V-doped compounds crystallize in the layered AlB_2 structure with a $P6/mmm$ hexagonal space group, where the Zr (or Hf) atoms and the B atoms occupy, respectively, the $1a$ (0,0,0) and $2d$ (1/3, 2/3, 1/2) positions. As in MgB_2, their crystal lattices are characterized by hexagonal metal layers alternating with graphite-like B layers (see Fig. 1).

Previous results of band-structure calculations [9,10] and Fermi surface (FS) representations [9] are available in the literature for both ZrB_2 and HfB_2. Since, however, the published FS of ZrB_2 suffers from low quality, we chose to present the result of our own calculation in Fig. 2, intended to serve as a comparison to the published FS in MgB_2 [11], well known for its amazingly high critical temperature T_c of the order of 40 K for the onset of superconductivity. Our density-functional calculations use a linear-density approximations (LDA) approach [12] based on the $DMol^3$ band-structure modeling program [13,14]. The self-consistent field (SCF) was accomplished using the standard double-numeric plus polarization (DNP) [13] variational basis set and a Γ-centered $12 \times 12 \times 12$ k mesh in the reciprocal cell. Pseudized scalar relativistic corrections [15] were applied. The calculations are based on the experimental geometries published in Ref. [16].

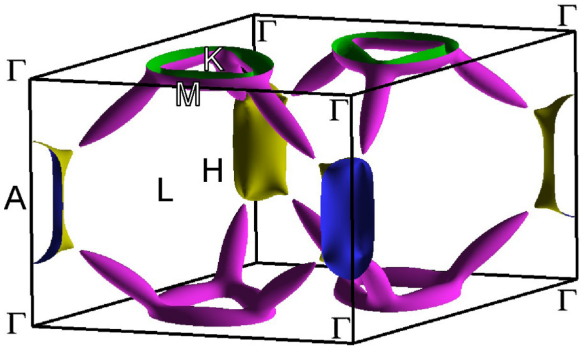

FIG. 2. Fermi surface of ZrB_2.

The FS plot was generated using the XCRYSDEN program [17] based on the $DMol^3$ output for a $99 \times 99 \times 99$ k mesh.

The ZrB_2 FS consists of four short cylindrical hole-type pockets around the A point and four tripod-shaped electron-type pockets, each consisting of a triangular ring around the K point and three elliptic extensions near the ΓAH plane. Since the FS of HfB_2 exhibits essentially the same features, we refrained from presenting it in a separate figure. These features are quite different from those of the FS of MgB_2. Most obvious is the reduction of the two almost two-dimensional hole sheets centered near the A point for MgB_2 to one much smaller and three-dimensional (3D) type pocket for Zr- and Hf-diboride. Likewise the 3D parts are quite different in shape for MgB_2. It is therefore not surprising that the two borides investigated here are less favorably conditioned for superconductivity than MgB_2 and indeed for both pure compounds, no superconductivity was detected above 1 K. The band-structure calculations for the T-borides considered here indicate that in both cases the density of electronic states at the Fermi energy $N(E_F)$ is located in a region where $N(E)$ exhibits a pseudogap, i.e., is much reduced. It is thus remarkable that a very small (4–5%) V-for-Zr or V-for-Hf substitution results in onsets of superconductivity up to approximately 8 K. More details on the crystal structure and defect-induced phase instabilities of these types of compounds are discussed in Ref. [7].

III. EXPERIMENTAL DETAILS

Polycrystals of ZrB_2, HfB_2, $Zr_{0.96}V_{0.04}B_2$, and $Hf_{0.97}V_{0.03}B_2$ were synthesized via boron carbide reduction and structurally characterized as described in Ref. [7]. For our magnetic measurements, samples in form of fine powders, with masses between 50 and 100 mg, were sealed in Teflon (PTFE) tubes. The NMR investigations including line-shape and spin-lattice relaxation measurements were performed in an applied magnetic field of 3.505 T since higher fields reduce the possibility to resolve the quadrupolar effects. In our case, the ^{11}B nucleus (spin $I = 3/2$) proved to be the most suitable one since it allows a direct comparison between the four samples and it is four times more abundant than ^{10}B. The NMR signals were monitored by means of standard spin-echo sequences, consisting in $\pi/2$ and π pulses of 2 and 4 μs, respectively, with recycle delays ranging from 10 to 100 s, for temperatures ranging from 4 to 295 K. The NMR lineshapes were obtained via the fast Fourier Transform (FFT) of the echo signal which, due to the high sensitivity of ^{11}B, could be acquired using relatively few scans (from 4 to 2048). The spin-lattice relaxation times T_1 were measured with the inversion recovery method, using a $\pi - \pi/2 - \pi$ pulse sequence. The magnetometry measurements were performed using a commercial Magnetic Property Measurement System (MPMS XL) from Quantum Design, equipped with a 7-T magnet and covering the temperature range from 2 to 400 K. For the resistivity measurements, the samples were densely packed in cylindrical pellets with a diameter of 1.4 mm and a thickness of 5 mm, produced by applying high external pressures. The electrical contacts with a four-probe configuration were made by means of an electrically conducting silver epoxy.

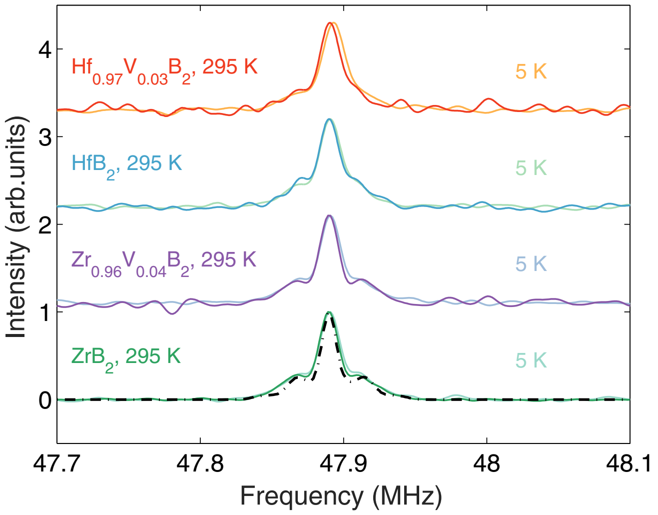

FIG. 3. ^{11}B NMR lines in the four TB_2 compounds, respectively. From bottom to top: ZrB_2, $Zr_{0.96}V_{0.04}B_2$, HfB_2, and $Hf_{0.97}V_{0.03}B_2$. The measurements were performed at 3.505 T and for each sample the lines measured at 5 and at 295 K are superposed, showing no relevant change. The dashed black line superposed on the ZrB_2 spectra represents a simulation of a $S = 3/2$ powder pattern with small quadrupole splitting (reflected by the two shoulders around the central transition).

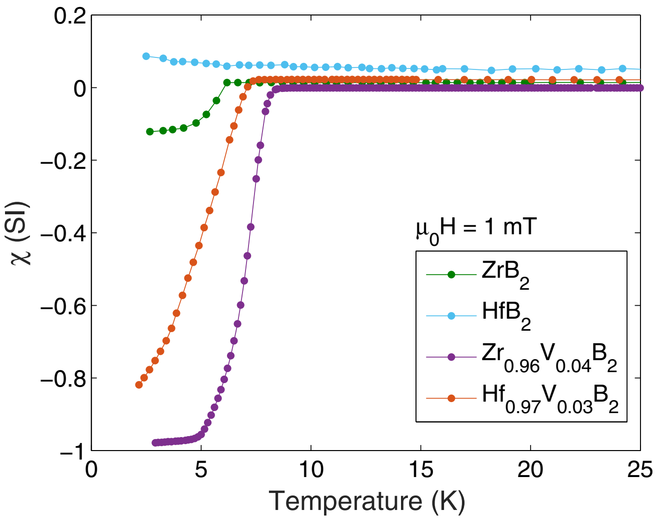

FIG. 4. Magnetic susceptibility data [$\chi(T)$ in SI units] at 1 mT for ZrB_2, HfB_2, $Zr_{0.96}V_{0.04}B_2$, and $Hf_{0.97}V_{0.03}B_2$. The undoped samples (and the doped ones above T_c) exhibit diamagnetic behavior (plateaux). Small ZrB_{12} impurities in ZrB_2 induce a superconducting transition at ~6 K. $Zr_{0.96}V_{0.04}B_2$ and $Hf_{0.97}V_{0.03}B_2$ become superconductors at $T_c = 8.33$ K and 7.31 K, respectively.

Preliminary μ^+SR measurements were made at the GPS spectrometer of the SμS facility of Paul Scherrer Institute (PSI) in Villigen, Switzerland. The available sample mass (300 mg) was sufficient to stop the 4-MeV muons without additional degraders and with a minimal background signal. To avoid pinning effects, well known for distorting the vortex lattice (VL) in the superconducting phase of MgB_2 [18], the transverse-field (TF) muon-spin rotation measurements were made at the highest field available (0.6 T).

IV. EXPERIMENTAL RESULTS AND DISCUSSION

A. Nuclear magnetic resonance

The ^{11}B NMR lines of all the samples (both pure and V-doped) were measured from 5 to 295 K; typical data are shown in Fig. 3. The reference ^{11}B NMR frequency in an applied magnetic field of 3.505 T was evaluated to be $\nu_0 = 47.8844$ MHz. In our case, the NMR lines exhibit peaks which are very close to the reference, with an absolute positive shift of only about 6 kHz, corresponding to a Knight shift of 120 ppm. In the covered temperature range between 5 and 295 K the ^{11}B NMR lines practically coincide (see Fig. 3), implying temperature-independent Knight shifts for all the measured samples, compatible with the $\chi(T)$ plateaux observed in the magnetometry data, measured under zero-field cooled conditions (see Fig. 4). The trend of the Knight shift in the superconducting phase could not be resolved because of the appreciable width of the resonance signal. As the line position, also the full width at half maximum (FWHM) is practically constant upon varying the temperature. For the Zr-based samples its value is 13 kHz (with 1 kHz of additional broadening below T_c), while for those containing Hf the width is 14 kHz (+1 kHz at low temperatures). The typical quadrupole splitting ν_Q in ZrB_2 and HfB_2 is approximately the same, i.e., 54 kHz. This relatively small value implies a rather small electric-field gradient (EFG), especially if compared with MgB_2, for which $\nu_Q \simeq 860$ kHz [19], which is a signature of a different electronic charge distribution, confirmed by the different orbitals involved in the bonds, i.e., only s and p orbitals for MgB_2 and also d orbitals for T-borides.

For typical powder spectra of a $I = 3/2$ nucleus with a small quadrupole splitting, an analytical expression for the lineshape can be derived by considering the quadrupole term as a first-order perturbation in the main Zeeman Hamiltonian [20,21]. As shown in Fig. 3, the experimental spectrum and the simulated lineshape (dashed line) for ZrB_2 agree quite well. The simulation of the powder spectrum, employing a MATLAB code, performs the integration according to Euler's method over all the possible orientations of the NMR lineshape factor F [20], i.e., the integration of the transition frequencies, derived from the quadrupolar theory and weighted using a Gaussian broadening function [22,23]. From a quantitative analysis, the electric-field gradient (EFG) tensor can be evaluated using

$$eq = \frac{2I(2I-1)\,h\nu_Q}{3eQ}, \qquad (1)$$

with eq the largest EFG component (parallel to the applied magnetic field), I the nuclear spin, and Q the quadrupole moment of the nucleus. By considering the hexagonal symmetry of the AlB_2 structure, we can assume that the in-plane anisotropy parameter $\eta = (V_{xx} - V_{yy})/V_{zz} = 0$ and, therefore, $V_{xx} = V_{yy}$. Since the $V_{i,j}$ tensor is traceless, by evaluating $eq = V_{zz}$ from the simulated ν_Q data [see Eq. (1)], we get $V_{zz} = 1.1 \times 10^{20}$ Vm^{-2} and $V_{xx} = V_{yy} = -5.5 \times 10^{19}$ Vm^{-2}.

TABLE I. Key NMR parameters for the investigated samples compared with those of AlB_2 and MgB_2 [24].

Material	Shift (ppm)	T_1T (10^4 s K)	S_0 (10^{-4} s K)
ZrB_2	120	1.81 ± 0.07	2.60 ± 0.18
$Zr_{0.96}V_{0.04}B_2$	120	1.89 ± 0.07	2.72 ± 0.11
HfB_2	140	1.67 ± 0.05	3.27 ± 0.12
$Hf_{0.97}V_{0.03}B_2$	140	1.56 ± 0.07	3.06 ± 0.09
AlB_2	–10	0.14 ± 0.04	0.009 ± 0.001
MgB_2	70	0.018 ± 0.006	0.009 ± 0.001

As summarized in Table I, the Knight shift values are of the same order of magnitude as in MgB_2 [19,24,26,27], but we note a difference of two orders of magnitude in the spin-lattice relaxation rates. The measured T_1T value for MgB_2 is 1.8×10^2 sK, which, by considering its 70 ppm Knight shift, implies an experimental Korringa constant $S_0 \equiv T_1TK^2 = 8.85 \times 10^{-7}$ sK, approximately three times smaller than the theoretical value $S_{\text{th}} = \hbar(\gamma_e/\gamma_B)^2/(4\pi k_B) = 2.56 \times 10^{-6}$ sK. Upon V doping, the very slow relaxation processes in T-diborides are nonsignificantly altered, but nevertheless, this apparently insignificant doping induces superconductivity at relatively high critical temperatures. Furthermore, due to strong covalent bonds, the largest contribution to the electronic density of states (DOS) at the Fermi level $D(E_F)$ is due to itinerant electrons in the boron layers. With respect to AlB_2 and even more so to MgB_2, $D(E_F)$ of our compounds is drastically reduced, as clearly confirmed by the spin-lattice relaxation data, in turn in good agreement with our theoretical calculations on the electronic structure of ZrB_2 and HfB_2.

The raw data, i.e., ^{11}B NMR T_1 inverse saturation recovery curves, for the temperatures above T_c were fitted by assuming the standard magnetization recovery formula for a single spin-lattice relaxation time [25]. However, due to the expected high anisotropy of $\mu_0 H_{c2}$, and by analogy with MgB_2 [5], in powder samples we expect grains with different orientations, i.e., where the applied magnetic field lies in the *ab* plane or is parallel to the *c* axis. *A priori* the orthogonal and parallel magnetic susceptibilities and the upper critical field depend on the direction of the field. The existence of nonequivalent grains, due to the anisotropy of the upper critical field, is also confirmed by magnetometry (Fig. 4) and resistivity (Fig. 8) measurements, which show a superconducting width transition $\Delta T \sim 2.5$ K, hence suggesting the persistence of inhomogenous domains. In a first approximation and following a procedure employed in the MgB_2 case [24,27], we can fit the data, by assuming two relaxation processes [see Eq. (2)], related to the normal phase and to the superconducting phase, respectively:

$$I(\tau_d) \propto \alpha \exp(\tau_d/T_{1s})^\beta + (1-\alpha)\exp(\tau_d/T_{1n})^\beta. \qquad (2)$$

Here τ_d is the time delay in the NMR pulse sequence, T_{1s} and T_{1n} the spin-lattice relaxation times of the superconducting and normal grains, respectively, α the superconducting volume fraction and β the stretching parameter (close to 1 in this case). We assume that α is a temperature-dependent fit parameter, ranging from $\sim$1 (in case of maximum superconducting fraction, as evaluated from magnetometry data), down to 0.

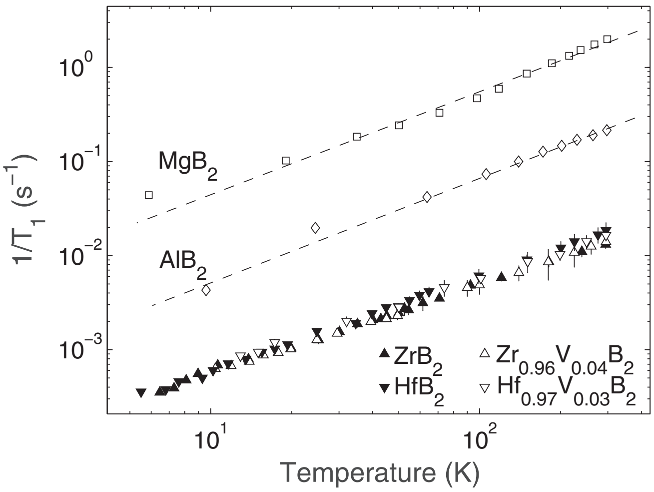

FIG. 5. ^{11}B NMR $T_1^{-1}(T)$ data at 3.505 T for all the investigated samples, compared to MgB_2 and AlB_2 data (from Ref. [24]). From a standard fit, assuming only one spin-lattice relaxation time [25], we obtain a linear trend, with Korringa constants as reported in Table I. Materials with transition metal cations, such as Zr and Hf, exhibit slow spin-lattice relaxation processes, two orders of magnitude slower than in MgB_2, whereas AlB_2 represents an intermediate case.

In the transition region the two plateaux are connected with a sigmoidal function.

The $T_1^{-1}(T)$ spin-lattice relaxation data above T_c follow the linear behavior in T of a simple metal (see Fig. 5), where nuclear relaxation occurs mostly via interactions with the conduction electrons. On the other hand, below T_c, the superconducting grains may exhibit two trends: a power-law with an integer exponent, typical of anisotropic superconductors, or an exponential trend, as expected for *s*-wave superconductors. If the sample is not perfectly homogeneous, a second relaxation component could persist as a linear trend associated to normal grains, as shown in Fig. 6. The hypothesis of the two relaxation times is justified by the good fit results that we obtain for the evaluation of spin-lattice relaxation rates $R_1 = T_1^{-1}$. A quantitative analysis is, however, hampered by a contribution to the relaxation from the flux vortex lines (i.e., their thermal motion) [28,29]. Since we performed a field cooling (FC) measurement, the formation of a flux line lattice (FLL) with a regular arrangement of vortices, most likely with hexagonal symmetry, is expected. The geometric parameter of this lattice is the intervortex spacing $d(\mu_0 H) = (2\Phi_0/3^{1/2}\mu_0 H)^{1/2}$, which implies $d(3.505T) = 26$ nm in our case. This value is approximately six times the diameter of the vortices ξ, as evaluated in Sec. IV C, implying that the measured T_1 values consist of the sum of a slow contribution from outside the vortex cores and a faster contribution from the normal region within the vortices [29].

We speculate that the considerable anisotropy of the upper critical field of MgB_2 [5] is also a characteristic of our materials. A rigorous confirmation would be obtained by relevant experiments on single crystals via, e.g., thermal conductivity measurements. In general, *s*-wave superconductors exhibit an exponential decrease of $T_1^{-1}(T)$ well below T_c, from which the gap value Δ can be extracted. The appearance of a Hebel-Slichter coherence peak is usually interpreted as

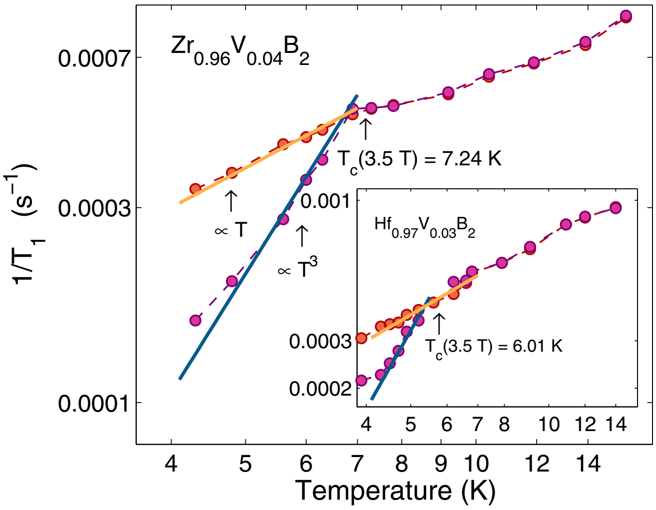

FIG. 6. ^{11}B NMR $1/T_1(T)$ data at 3.505 T for Zr$_{0.96}$V$_{0.04}$B$_2$ (main plot) and Hf$_{0.97}$V$_{0.03}$B$_2$ (inset), representing the two relaxation times of Eq. (2), which result from fitting the inversion recovery curves. Both superconducting samples exhibit a conventional metallic trend (red points) and a superconducting dropdown (magenta points). The blue lines are power laws with critical exponent 3, that would be a signature of d-wave superconductivity. In both samples we argue that the faster relaxation rates below 5.5 K with respect to the power-law support the hypothesis of s-wave pairing.

confirming the Cooper-pairing with spherical symmetry. In our case, the absence of a coherence peak does not rule out an s-wave parity since the size of the peak can be significantly reduced by the pair-breaking mechanism in the presence of high fields [30]. Due to the above-mentioned complexity of the relaxation processes and the quality of our data, it is impossible to extract the gap value Δ from the exponential decrease of the spin-lattice relaxation time. In any case, a first evidence for s-wave superconductivity is the increasing deviation from a power-law behavior with an exponent 3 towards lower temperatures (see Fig. 6). To justify the similarities between the phonon-mediated s-wave superconductivity mechanism in MgB$_2$ and our V-doped samples we note that vanadium, given its $3d^3$ orbital, has one more electron, if compared to Zr ($4d^2$) and Hf ($5d^2$). An analogous electron doping is confirmed in the case of MgB$_2$, where the s states of Mg are pushed up by the boron p_z orbitals and, therefore, fully donate their electrons to the boron-derived conduction band [4]. This doping mechanism occurs also in the opposite direction (reduction of the T_c value) in MgB$_2$. In this case, both the substitution of Mg with Li (hole doping) and of boron with carbon or Al (electron doping) reduce the T_c of the material [31]. In this case, it is claimed that the electrons fill the σ band and holes occupy the π band, therefore making charge compensation impossible. Furthermore, a recent paper [32] supported the hypothesis of two gaps in Zr$_{0.96}$V$_{0.04}$B$_2$ from critical current density J_c measurements in different fields. In fact, J_c can suitably be fitted by the sum of two contributions J_1 and J_2, respectively, related to the first and the second gap, following an exponential trend as a function of the applied magnetic field.

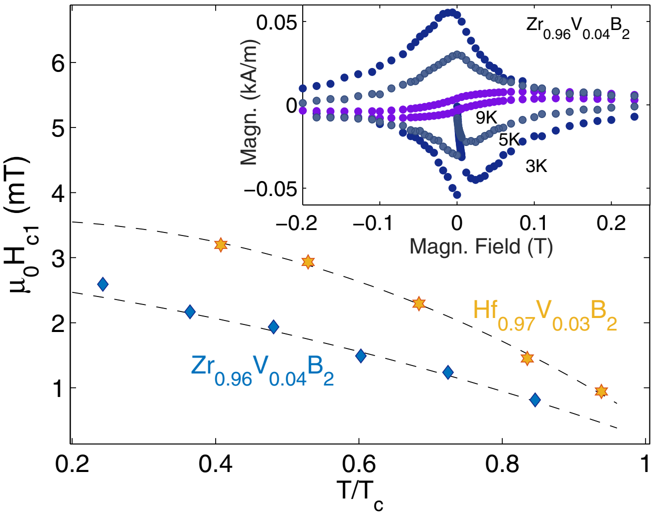

FIG. 7. The temperature dependence of $\mu_0 H_{c1}$ exhibits a negative curvature. By using parabolic fits (dashed lines) the approximate $H_{c1}(0)$ values are obtained: 2.5 mT for Zr$_{0.96}$V$_{0.04}$B$_2$ and 3.6 mT for Hf$_{0.97}$V$_{0.03}$B$_2$. Inset: the M vs. H plots (zero field cooling) in Zr$_{0.96}$V$_{0.04}$B$_2$ at 3, 5, and 9 K.

B. Magnetometry

Superconducting quantum interference device (SQUID) magnetometry measurements were made on all the samples (ZrB$_2$, HfB$_2$, Zr$_{0.96}$V$_{0.04}$B$_2$, and Hf$_{0.97}$V$_{0.03}$B$_2$). The high sensitivity (10^{-10} Am^2) of the reciprocating sample option (RSO) of the MPMS magnetometer allowed us to detect small impurities. In particular, in the ZrB$_2$ and Zr$_{0.96}$V$_{0.04}$B$_2$ samples a small mass fraction of about 0.5 % exhibits a superconducting transition at 5.5 K, the typical T_c of ZrB$_{12}$ impurities. Smaller impurity contributions are also visible from the $\chi(T)$ plots at fields between 0.1 and 7 T, exhibiting a steady increase below 20 K. Therefore, an accurate measurements of $T_c(H = 0)$ was achieved by applying a small magnetic field of 1 mT. The obtained values of T_c are 8.33 K for Zr$_{0.96}$V$_{0.04}$B$_2$ and 7.31 K for Hf$_{0.97}$V$_{0.03}$B$_2$. As shown in the inset of Fig. 7, the typical type-II SC cycles can be observed below T_c; above T_c, a clear diamagnetic trend is confirmed with a typical $\chi_m = -7.5 \times 10^{-10}$ m^{3}mol^{-1}, a value approximately five times smaller than bismuth.

The low-field region (from 0.2 to 6 mT), exhibits an initial linear trend in $M(H)$. It is possible to extract an approximate value of $\mu_0 H_{c1}$, defining it as the field at which the deviation from the linear trend (called *Meissner line*) exceeds the sensitivity of the instrument. Performing this analysis, for each of the M versus H curves, we obtain $\mu_0 H_{c1}(T)$, as shown in Fig. 7 for both Zr$_{0.96}$V$_{0.04}$B$_2$ and Hf$_{0.97}$V$_{0.03}$B$_2$. According to the two-band Ginzburg-Landau theory applied to MgB$_2$, the lower critical field exhibits a change in concavity (from negative to positive, upon cooling) at $T/T_c \sim 0.5$ [33]. Since this change is scarcely distinct and the model depends upon the interband mixing of the two order parameters and of their gradients, it is difficult to interpret the $\mu_0 H_{c1}(T)$ trend which, as reported in the literature for MgB$_2$ [34,35] can be fitted even with a line. On the other hand, the previously reported Zr$_{0.96}$V$_{0.04}$B$_2$ data [7] show a pronounced upturn, which is not

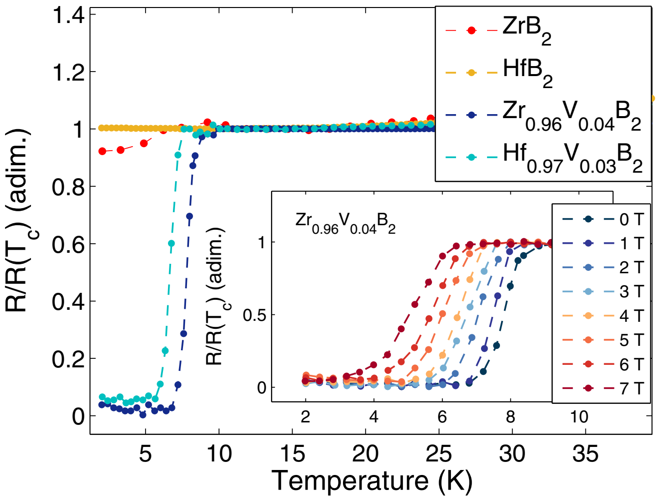

FIG. 8. R vs. T data for all the samples (ZrB_2, HfB_2, $Zr_{0.96}V_{0.04}B_2$, and $Hf_{0.97}V_{0.03}B_2$) in zero field. The superconducting dropdown in $Zr_{0.96}V_{0.04}B_2$ and $Hf_{0.97}V_{0.03}B_2$ are evident and confirm the SQUID magnetometry measurement. On the other hand, undoped samples exhibit a constant plateau, as reflected also by the constance of Knight shift (see Sec. IV A). We attribute the small dropdown of ZrB_2 to ZrB_{12} impurities. The inset shows the resistivity data of $Zr_{0.96}V_{0.04}B_2$ between 2 and 35 K has been measured at different fields (from 0 to 7 T), confirming a reduced steepness towards higher fields (ΔT ranging from 2.5 to 3.5 K towards higher fields) and the expected negative shift.

present in our case. The reason for this discrepancy is unclear at the moment.

C. Resistivity

Systematic resistivity measurements were performed in zero field on all the samples (ZrB_2, HfB_2, $Zr_{0.96}V_{0.04}B_2$, and $Hf_{0.97}V_{0.03}B_2$), as shown in Fig. 8, and on the superconducting samples $Zr_{0.96}V_{0.04}B_2$ (see the inset of Fig. 8) and $Hf_{0.97}V_{0.03}B_2$ in magnetic fields up to 7 T.

Each resistance measurements in zero field (ZF) was performed from 2 to 310 K, while in field we focused our attention on the superconducting transition region (range from 2 to 10 K). Due to the small resistivity values, i.e., $\rho(T_c) \sim 0.7\ \mu\Omega$cm for $Zr_{0.96}V_{0.04}B_2$ and $0.8\ \mu\Omega$cm for $Hf_{0.97}V_{0.03}B_2$, we argue that we can analyze our data within the clean limit approximation.

Based on the data at different fields, the $\mu_0 H_{c2}(T)$ values were evaluated (see Fig. 9). According to the theory of Werthamer, Helfand, and Hohenberg (WHH) [36], in the clean limit [37] and for small spin-orbit couplings [38] we have

$$\mu_0 H_{c2}(0) = -0.73\, T_c \left.\frac{dH_{c2}}{dT}\right|_{T=T_c}. \qquad (3)$$

Within this approximation, $\mu_0 H_{c2}(T_c)$ can be fitted with a parabolic curve

$$\mu_0 H_{c2}(T) = \mu_0 H_{c2}(0)\,[1-(T/T_c)^2]. \qquad (4)$$

From the Ginzburg-Landau formula $\xi(0) = [\phi_0/(2\pi \mu_0 H_{c2}(0))]^{1/2}$, our estimate of the coherence lengths $\xi(0)$ in both $Zr_{0.96}V_{0.04}B_2$ and $Hf_{0.97}V_{0.03}B_2$ are 4.5(1) and 5.5(1) nm, respectively. By numerically solving

$$\frac{\mu_0 H_{c2}(0)}{\mu_0 H_{c1}(0)} = \frac{2\kappa^2}{\ln \kappa}, \qquad (5)$$

we finally obtain the Ginzburg-Landau κ parameter, with a value of 125 for $Zr_{0.96}V_{0.04}B_2$ and 80 for $Hf_{0.97}V_{0.03}B_2$, respectively, indicating the strong type-II nature of these superconductors. From $\kappa = \lambda/\xi$, the London penetration depth $\lambda(0)$ in the two materials, is 570 and 445 nm, respectively.

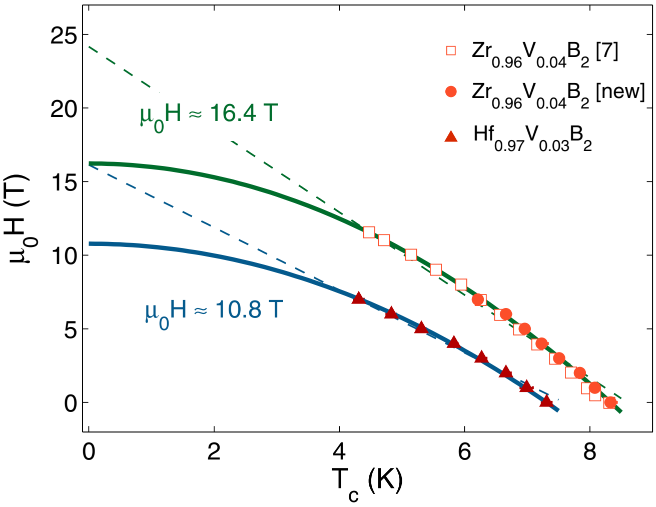

FIG. 9. $\mu_0 H_{c2}(T_c)$ plots for $Zr_{0.96}V_{0.04}B_2$ (filled orange circles) and $Hf_{0.97}V_{0.03}B_2$ (filled red triangles) are derived from resistivity measurements at different field from 0 to 7 T. Via the WHH model, that implies a parabolic fit (green and blue continuous lines), we can evaluate $\mu_0 H_{c2}(0)$, i.e., 16.4 T for $Zr_{0.96}V_{0.04}B_2$ and 10.8 T for $Hf_{0.97}V_{0.03}B_2$. Since Hf is heavier than Zr, we argue that the lower value in the upper critical field is related to the lower average phonon frequency. The old data (Ref. [7], empty squares) and the new ones (circles) are in good agreement.

D. Muon-spin rotation results in the SC phase

Values of similar magnitude for the magnetic field penetration depth were obtained from preliminary muon-spin rotation (μSR) experiments on $Zr_{0.96}V_{0.04}B_2$ (see Fig. 10). Once implanted in matter, spin-polarized muons act as microscopic probes of magnetism, which upon decay emit positrons preferentially along the muon-spin direction. From the spatial anisotropy of the emitted positrons (i.e., the asymmetry signal) one can reveal the distribution of the local magnetic fields [39,40]. In our case, by applying 0.6 T, a regular flux-line lattice (FLL) develops in the superconducting phase below T_c. By uniformly sampling the FLL, muons experience an additional relaxation σ_{sc}, which is related to the absolute magnetic penetration depth λ via [41,42]

$$\frac{\sigma_{sc}^2}{\gamma_\mu^2} = 0.00371 \cdot \frac{\Phi_0^2}{\lambda^4}. \qquad (6)$$

Here $\Phi_0 = 2.068 \times 10^{-3}\ \mathrm{T}\mu\mathrm{m}^2$ is the magnetic flux quantum and $\gamma_\mu = 2\pi \times 135.53$ MHz/T, the muon gyromagnetic ratio.

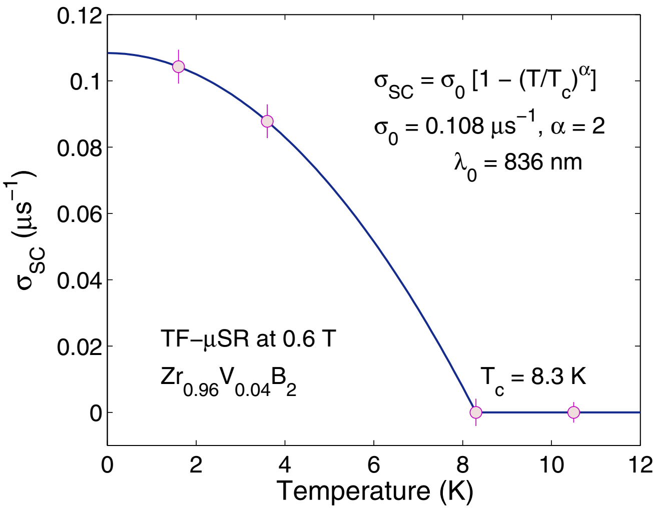

FIG. 10. Transverse-field $\mu_S R$ data in the superconducting phase of $Zr_{0.96}V_{0.04}B_2$ in a magnetic field $\mu_0 H = 0.6$ T.

Figure 10 shows the temperature dependence of σ_{sc}, proportional to the superfluid density [$\sigma_{sc} \propto n_s \propto \lambda^{-2}(T)$], together with a numerical fit with an average-field model $1/\lambda^2(T) = [1/\lambda^2(0)][1 - (T/T_c)^n]$, which gives $1/\lambda^2(0) = 1.43 \pm 0.2\ \mu\mathrm{m}^{-2}$ and $n = 2.0 \pm 0.1$. Subsequently, by using the relation $\lambda_{ab}(0) = \lambda_{\mathrm{eff}}(0)/1.31$, we estimate the in-plane magnetic penetration depth $\lambda_{ab}(0) = 638 \pm 11$ nm. This value is close to the one determined via macroscopic methods (see above), but it is very different from $\lambda_{ab}(0) = 100$ nm, also measured via μSR in MgB_2 [18]. This difference can be accounted for by considering the rather small electronic density of states in $Zr_{0.96}V_{0.04}B_2$ compared to that in MgB_2, compatible with the very different NMR relaxation-rate values reported in Table I.

As a final note, we recall that the choice of the applied transverse field is crucial for the correct determination of the field penetration depth. Indeed, detailed studies of the magnetic field dependence of the muon-spin depolarization rate in MgB_2 (see, e.g., Figs. 1 and 2 in Ref. [18]) have shown strong pinning effects in low applied fields (below 0.3 T). These imply a considerably distorted vortex lattice leading to a strong decay of the muon asymmetry and hence underestimated $\lambda_{ab}(0)$ values. However, since in fields exceeding 0.3 T, only weak or no pinning effects were observed, we are confident that by applying a transverse field of 0.6 T, our results reflect the penetration depth.

V. SUMMARY AND CONCLUSION

From SQUID magnetometry, NMR, resistivity, and preliminary μSR experiment data on ZrB_2, HfB_2, $Zr_{0.96}V_{0.04}B_2$, and $Hf_{0.97}V_{0.03}B_2$, we argue that the latter two samples are s-wave superconductors, resulting from electron doping via d orbitals of vanadium. On the other hand, in MgB_2 the peculiar self-doping exists thanks to the boron-related electrons at the Fermi level; at the same time also the s states of Mg donate their electrons to the boron-derived conduction bands (*metallic* B). It is also worth mentioning that B vacancies (a common defect occurring in diborides) enhance the DOS even further (more than twice for doping of about 0.5%) [8]. Besides the many similarities with MgB_2, the lower T_c values (7.31 and 8.33 K instead of 39 K) are accounted for by the differences in the electronic structure and Fermi surface. The DOS per unit cell of MgB_2 at the Fermi level (0.719 states/eV) is dominated (about 60%) by the p orbitals of B atoms, while in the case of the undoped transition-metal diborides (ZrB_2, for instance) 80% of the DOS (0.130 states/eV) [9] derives from the d orbitals of the cation. Furthermore, our data support the hypothesis that we are dealing with new two-band two-gap s-wave superconductors, since the coexistence of a normal and a superconducting phase below T_c suggests an anisotropy of the upper critical field, as is well documented in the paradigmatic case of MgB_2. More direct evidence for this assumption could be obtained by various experiments probing single crystals of $Zr_{0.96}V_{0.04}B_2$ and $Hf_{0.97}V_{0.03}B_2$.

ACKNOWLEDGMENT

This work was financially supported in part by the Schweizerische Nationalfonds zur Förderung der Wissenschaftlichen Forschung (SNF).

---

[1] W. Meissner and H. Franz, Supraleitfähigkeit von Carbiden und Nitriden, Naturwissenschaften **18**, 418 (1930).

[2] R. Hott, R. Kleiner, Th. Wolf, and G. Zwicknagl, Review on superconducting materials, in *Digital Encyclopedia of Applied Physics*, edited by R. K. Harris and R. E. Wasylishen (Wiley-VCH Verlag GmbH & Co. KGaA, Hoboken, NJ, 2016).

[3] J. Nagamatsu, N. Nakagawa, T. Muranaka, Y. Zenitani, and J. Akimitsu, Superconductivity at 39 K in magnesium diboride, Nature (London) **410**, 63 (2001).

[4] J. Kortus, I. I. Mazin, K. D. Belashchenko, V. P. Antropov, and L. L. Boyer, Superconductivity of Metallic Boron in MgB_2, Phys. Rev. Lett. **86**, 4656 (2001).

[5] A. V. Sologubenko, J. Jun, S. M. Kazakov, J. Karpinski, and H.-R. Ott, Temperature dependence and anisotropy of the bulk upper critical field H_{c2} of MgB_2, Phys. Rev. B **65**, 180505 (2002).

[6] R. Heid, B. Renker, H. Schober, P. Adelmann, D. Ernst, and K.-P. Bohnen, Lattice dynamics and electron-phonon coupling in transition-metal diborides, Phys. Rev. B **67**, 180510 (2003).

[7] S. T. Renosto, H. Consoline, C. A. M. dos Santos, J. Albino Aguiar, S.-G. Jung, J. Vanacken, V. V. Moshchalkov, Z. Fisk, and A. J. S. Machado, Evidence of multiband behavior in the superconducting alloy $Zr_{0.96}V_{0.04}B_2$, Phys. Rev. B **87**, 174502 (2013).

[8] M. Dahlqvist, U. Jansson, and J. Rosen, Influence of boron vacancies on phase stability, bonding and structure of MB_2 (M = Ti, Zr, Hf, V, Nb, Ta, Cr, Mo, W) with AlB_2 type structure, J. Phys.: Condens. Matter **27**, 435702 (2015).

[9] I. R. Shein and A. L. Ivanovskii, Band structure of ZrB_2, VB_2, NbB_2, and TaB_2 hexagonal diborides: Comparison with superconducting MgB_2, Phys. Solid State **44**, 1833 (2002).

[10] G. E. Grechnev, A. V. Fedorchenko, A. V. Logosha, A. S. Panfilov, I. V. Svechkarev, V. B. Filippov, A. B. Lyashchenko, and A. V. Evdokimova, Electronic structure and magnetic properties of transition metal diborides, J. Alloys Compd. **481**, 75 (2009).

[11] I. I. Mazin and V. P. Antropov, Electronic structure, electron–phonon coupling, and multiband effects in MgB_2, Phys. C: Supercond. **385**, 49 (2003).

[12] J. P. Perdew and Y. Wang, Accurate and simple analytic representation of the electron-gas correlation energy, Phys. Rev. B **45**, 13244 (1992).

[13] B. Delley, An all-electron numerical method for solving the local density functional for polyatomic molecules, J. Chem. Phys. **92**, 508 (1990).

[14] B. Delley, From molecules to solids with the $DMol^3$ approach, J. Chem. Phys. **113**, 7756 (2000).

[15] B. Delley, A scattering theoretic approach to scalar relativistic corrections on bonding, Int. J. Quant. Chem. **69**, 423 (1998).

[16] L. Bsenko and T. Lundström, The high-temperature hardness of ZrB_2 and HfB_2, J. Less Common Metals **34**, 273 (1974).

[17] A. Kokalj, XCrySDen—a new program for displaying crystalline structures and electron densities, J. Mol. Graph. Model. **17**, 176 (1999).

[18] Ch. Niedermayer, C. Bernhard, T. Holden, R. K. Kremer, and K. Ahn, Muon spin relaxation study of the magnetic penetration depth in MgB_2, Phys. Rev. B **65**, 094512 (2002).

[19] G. Papavassiliou, M. Pissas, M. Fardis, M. Karayanni, and C. Christides, ^{11}B NMR detection of the magnetic field distribution in the mixed superconducting state of MgB_2, Phys. Rev. B **65**, 012510 (2001).

[20] R. Goc and D. Fiat, NMR powder spectrum simulation for nuclei with $I > 1/2$, Phys. Status Solidi (B) **140**, 243 (1987).

[21] M. H. Cohen, Nuclear quadrupole spectra in solids, Phys. Rev. **96**, 1278 (1954).

[22] D. W. Alderman, M. S. Solum, and D. M. Grant, Methods for analyzing spectroscopic line shapes. NMR solid powder patterns, J. Chem. Phys. **84**, 3717 (1986).

[23] P. Hodgkinson and L. Emsley, Numerical simulation of solid-state NMR experiments, Prog. Nucl. Magn. Reson. Spectrosc. **36**, 201 (2000).

[24] S. H. Baek, B. J. Suh, E. Pavarini, F. Borsa, R. G. Barnes, S. L. Bud'ko, and P. C. Canfield, NMR spectroscopy of the normal and superconducting states of MgB_2 and comparison to AlB_2, Phys. Rev. B **66**, 104510 (2002).

[25] A. F. McDowell, Magnetization recovery curves for quadrupolar spins, J. Magn. Reson., Ser. A **113**, 242 (1995).

[26] H. Kotegawa, K. Ishida, Y. Kitaoka, T. Muranaka, and J. Akimitsu, Evidence for Strong-Coupling s-Wave Superconductivity in MgB_2: ^{11}B NMR Study, Phys. Rev. Lett. **87**, 127001 (2001).

[27] E. Pavarini, S. H. Baek, B. J. Suh, F. Borsa, S. L. Bud'ko, and P. C. Canfield, NMR relaxation rates and Knight shifts in MgB_2 and AlB_2: Theory versus experiments, Supercond. Sci. Tech. **16**, 147 (2003).

[28] J. K. Jung, S. H. Baek, F. Borsa, S. L. Bud'ko, G. Lapertot, and P. C. Canfield, ^{11}B NMR and relaxation in the MgB_2 superconductor, Phys. Rev. B **64**, 012514 (2001).

[29] A. Rigamonti, F. Borsa, and P. Carretta, Basic aspects and main results of NMR-NQR spectroscopies in high-temperature superconductors, Rep. Progr. Phys. **61**, 1367 (1998).

[30] Y. Masuda and N. Okubo, Nuclear spin-lattice relaxation in superconducting mixed state, J. Phys. Soc. Jpn. **26**, 309 (1969).

[31] J. Karpinski, N. D. Zhigadlo, S. Katrych, K. Rogacki, B. Batlogg, M. Tortello, and R. Puzniak, MgB_2 single crystals substituted with Li and with Li-C: Structural and superconducting properties, Phys. Rev. B **77**, 214507 (2008).

[32] S.-G. Jung, J. Vanacken, V. V. Moshchalkov, S. T. Renosto, C. A. M. dos Santos, A. J. S. Machado, Z. Fisk, and J. Albino Aguiar, Critical current density and flux pinning in $Zr_{0.96}$ $V_{0.04}$ B_2 superconductor with AlB_2 structure, J. Appl. Phys. **114**, 133905 (2013).

[33] I. N. Askerzade, A. Gencer, and N. Güçlü, On the Ginzburg-Landau analysis of the upper critical field H_{c2} in MgB_2, Supercond. Sci. Technol. **15**, L13 (2002).

[34] A. Sharoni, I. Felner, and O. Millo, Tunneling spectroscopy and magnetization measurements of the superconducting properties of MgB_2, Phys. Rev. B **63**, 220508 (2001).

[35] S. L. Li, H. H. Wen, Z. W. Zhao, Y. M. Ni, Z. A. Ren, G. C. Che, H. P. Yang, Z. Y. Liu, and Z. X. Zhao, Linear temperature dependence of lower critical field in MgB_2, Phys. Rev. B **64**, 094522 (2001).

[36] E. Helfand and N. R. Werthamer, Temperature and purity dependence of the superconducting critical field, H_{c2}. II, Phys. Rev. **147**, 288 (1966).

[37] S. Khim, B. Lee, J. W. Kim, E. S. Choi, G. R. Stewart, and K. H. Kim, Pauli-limiting effects in the upper critical fields of a clean LiFeAs single crystal, Phys. Rev. B **84**, 104502 (2011).

[38] N. R. Werthamer, E. Helfand, and P. C. Hohenberg, Temperature and purity dependence of the superconducting critical field, H_{c2}. III. Electron spin and spin-orbit effects, Phys. Rev. **147**, 295 (1966).

[39] S. J. Blundell, Spin-polarized muons in condensed matter physics, Contemp. Physics **40**, 175 (1999).

[40] A. Yaouanc and P. Dalmas de Réotier, *Muon Spin Rotation, Relaxation, and Resonance: Applications to Condensed Matter* (Oxford University Press, Oxford, 2011).

[41] E. H. Brandt, Flux distribution and penetration depth measured by muon spin rotation in high-T_c superconductors, Phys. Rev. B **37**, 2349 (1988).

[42] E. H. Brandt, Properties of the ideal Ginzburg-Landau vortex lattice, Phys. Rev. B **68**, 054506 (2003).